JOURNAL OF GUIDANCE, CONTROL, AND DYNAMICS
Vol. 31, No. 3, May–June 2008

Measuring and Modeling the Dynamics of Stiffened Thin-Film Polyimide Panels

Jonathan T. Black* and Suzanne Weaver Smith†
University of Kentucky, Lexington, Kentucky 40506
Jack Leifer‡
Trinity University, San Antonio, Texas 78212
and
Larry Bradford§
Energy Engineering, Holly Pond, Alabama 35083

DOI: 10.2514/1.32236

Stiff, ultralightweight thermal-formed polyimide panels are examples of next-generation space structures that address some of the issues of membrane-dominated ultralightweight structures while maintaining their low mass and low stowage volume characteristics. The research presented here involved dynamically characterizing and modeling two of these panels, one 0.0625 m^2 with a mass of 38 g and the other 0.1875 m^2 with a mass of 81 g, to develop validated computer models that can be used to determine the effects of changing manufacturing parameters and scalability. Modal testing using an impact hammer and accelerometer extracted the first four structural natural frequencies, the first occurring at 71.9 Hz. These data were replicated by simple, coarsely meshed shell element finite element models that are significantly smaller than previous finite element models of similar structures.

Nomenclature

E_x = modulus of elasticity along the major axis
E_y = modulus of elasticity along the minor axis
E_{app} = apparent modulus of a hollow beam
ℓ = hexagonal void edge length
t = hexagonal void spacing
ζ = damping coefficient of the system
θ = internal angle of hexagonal stiffeners
ρ = volumetric density
ν_{ij} = generic Poisson's ratio

I. Introduction

STIFF, thermal-formed thin-film polyimide panels are part of a unique class of structures that seek to mitigate some of the modeling and testing complications presented by other flexible and highly nonlinear ultralightweight membrane structures. Figure 1 shows two examples of different geometries of these panels. The ability to customize the thickness, stiffness, mass, and size of the panels and to connect multiple panels in any configuration may enable their use in solar arrays, flat panel optics, and space habitats, among others. However, to perform optimally in these very different applications, a detailed characterization of these panels is essential. This paper examines the global dynamic behavior of stiff, thermal-formed thin-film polyimide panels and validates novel numerical models that capture the behavioral mechanics of the panels. The work presented here is a continuation of the work presented in Black et al. [1], and part of an overall effort to characterize the static and dynamic behavior of these panels [2].

Although inflatable and/or rigidizable space structures have recently been extensively investigated [3–5], formed or stiffened membrane structures have received substantially less attention. Flint et al. [6,7] examined "doubly-curved form stiffened thin-film shells" in which the membrane was manufactured such that, without adding mass, the final surface had permanent depth and curvature. Song et al. [8] investigated a membrane torus with a 1.8 m ring diameter and a 0.2 m tube diameter. Unlike similar tori investigated in Griffith and Main [9] and Ruggiero et al. [10], a regular pattern of convex hexagonal domes 8 mm side to side and 3.5 mm high was formed into the polyimide film from which the torus was constructed. These domes provided a stiffness that enabled the structure to be self-supporting, and are comparable to the tessellating thermal-formed honeycomb pattern visible in Fig. 1 that provides the stiffness of the polyimide panels examined here.

In Lore and Smith [11], a technique used extensively in the automotive industry for computing the solution of structural dynamic models potentially millions of degrees of freedom in size was applied to models of thermal-formed membrane structures such as the torus tested in Song et al. [8]. This technique, called automated multilevel substructuring (AMLS) [12], is amenable to parallelization and required substantially less computing time than a Lancoz solver for a 500,000-degrees-of-freedom model from which 275 modes were extracted.

In small-scale compression testing of the panels shown in Fig. 1, significant nonlinear stiffness behavior was observed. To model this behavior, the stiffness of nonlinear springs was previously defined to match that measured experimentally, producing models that quite faithfully replicated experimental data. Modeling full-sized panels with this approach, however, also yields model sizes on the order of hundreds of thousands of degrees of freedom requiring significant computational effort [1,2]. Because of the disappearance of the observed small-scale local nonlinear behavior at the full-panel scale, the use of linear shell element models is appropriate [1,2]. An alternate modeling approach is therefore proposed here in which the internal honeycomb structure is approximated in the bulk material properties and the panels are assumed to be solid plates that can be coarsely meshed, eliminating the need for finely meshed models

---

Presented as Paper 1833 at the 48th AIAA/ASME/ASCE/AHS/ASC Structures, Structural Dynamics, and Materials Conference, Honolulu, Hawaii, 23–26 April 2007; received 8 June 2007; revision received 9 October 2007; accepted for publication 9 October 2007.

[*] Ph.D. Student; Currently Assistant Professor, Air Force Institute of Technology. Member AIAA.

[†] Lester Professor of Mechanical Engineering, 151 Ralph G. Anderson Building. Fellow AIAA.

[‡] Assistant Professor, Department of Engineering Science, One Trinity Place. Member AIAA.

[§] President, 1811 County Road 1740. Member AIAA.

Fig. 1 **Examples of stiff thermal-formed polyimide panels.**

hundreds of thousands of degrees of freedom in size used in the previous studies.

The initial step in the dynamic characterization and modeling of stiff, thermal-formed thin-film polyimide panels was to determine which excitation method would be used in the modal testing. The rectangular panel shown in Fig. 1 and an array of three of those rectangular panels attached to one another were dynamically characterized using two different methods, and coarsely meshed shell element models were used to replicate the data.

II. Excitation Method

Unique next-generation stiffened membrane structures, such as the thermal-formed polyimide panels studied here, present unique testing challenges. Song et al. [8] state: "In this project the unpressurized torus structure is far too flexible to be excited with any solid contact excitation: it simply crumpled under the force. Therefore, impact hammers and shakers simply will not work as methods of excitation. To overcome this drawback, acoustic excitation from a loudspeaker was used to excite the torus." Despite the previous success of acoustic testing methods in characterizing the dynamic behavior of similar stiff, ultralightweight membrane structures, they proved inadequate in the full-panel testing described next due to an insufficient dynamic range of the speaker and difficulty achieving response amplitudes sufficiently greater than the background noise of the measurement system. The much greater local stiffness of the current panels in comparison to the torus tested acoustically in Song et al. [8] enabled more traditional impact hammer testing to be successful here. Resulting natural frequencies and mode shapes were used to develop the simple coarsely meshed shell element models.

Impact or impulse excitation was not used in the tests described in Song et al. [8] due to the extreme flexibility of the self-supporting torus. The panels tested here, however, exhibit a much greater local stiffness than that torus, and do not crumple under moderate local impacts. They are also stiff enough to enable the attachment of small accelerometers to the panel surface without significantly altering their stiffness properties. Therefore, instead of the noncontact acoustic testing necessary for the characterization of other gossamer-class structures, a more traditional modal test was able to be performed in which an impulse hammer excited the panels and their response was measured by attached accelerometers.

In the impact hammer results below, a hard, steel-tipped hammer was used to excite the structure because it provides the greatest input frequency range and has a flat instead of a pointed tip. The flat steel tip spreads the force of the impact out over the entire surface area of the tip instead of concentrating it at a point that may have overloaded and damaged a local area of the thin polyimide membrane of which the panels are comprised.

An example of actual measured time history data using the steel-tipped impact hammer is shown in Fig. 2. The top graph shows the excitation impulse supplied by the hammer, and the bottom graph shows the response of the structure measured by the attached accelerometer. The excitation impulse appears almost ideal, with no evidence of multiple peaks that would indicate multiple hits. The structural response is well above the noise floor of the accelerometer, and exponentially decaying as expected in impact testing.

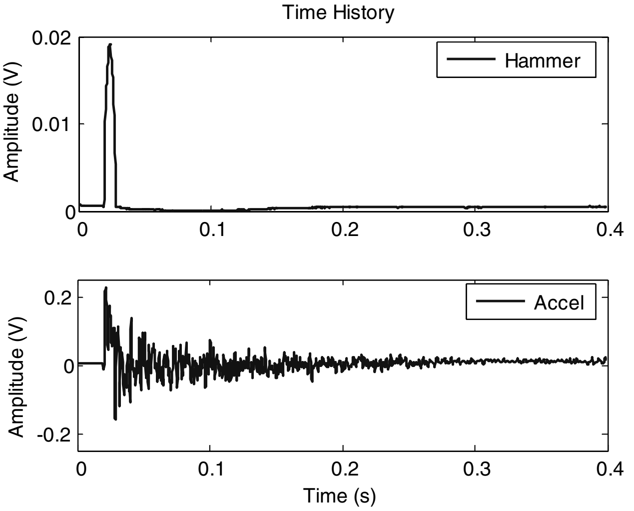

Fig. 2 **Example of measured time history data from the impact hammer test of a rectangular panel.**

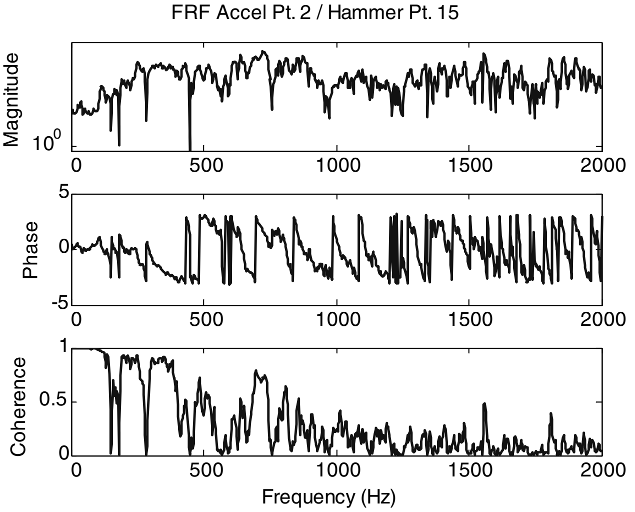

Fig. 3 **Example of the frequency response function from the impact hammer test of a rectangular panel.**

Figure 3 shows the frequency response function (FRF) created by relating the known excitation to the known response in the top and bottom graphs of Fig. 2, respectively. Data from 20 impacts at the same point were averaged together here. This FRF is obviously quite noisy, a symptom of the panel's nonlinear behavior (see the reciprocity test next), but peaks or dips in the magnitude corresponding to phase shifts and dips in coherence are clearly visible. These indicate that structural natural frequencies can be identified from the data. Also of note is that the coherence is close to 1 from approximately 0–400 Hz (Fig. 4). Impact hammer testing should therefore be capable of identifying the structural resonance frequencies and mode shapes of the stiff, ultralightweight polyimide panels over this frequency range. These results are detailed in the next section.

A reciprocity test was performed to examine the nonlinear behavior of the panel and the quality of the impact hammer measurements, and is shown in Fig. 5. As will be discussed next, two separate data runs were performed with the accelerometer attached at excitation point 2 in the first and point 19 in the second. One of the FRFs in Fig. 5 was therefore calculated from the first "a" data run impacting at point 19, creating the condition in which point 2 was the known response and point 19 was the known excitation; the second was calculated from the second "b" data run impacting at point 2, creating the reciprocal condition in which point 19 was the known response and point 2 was the known excitation. Reciprocity tests of

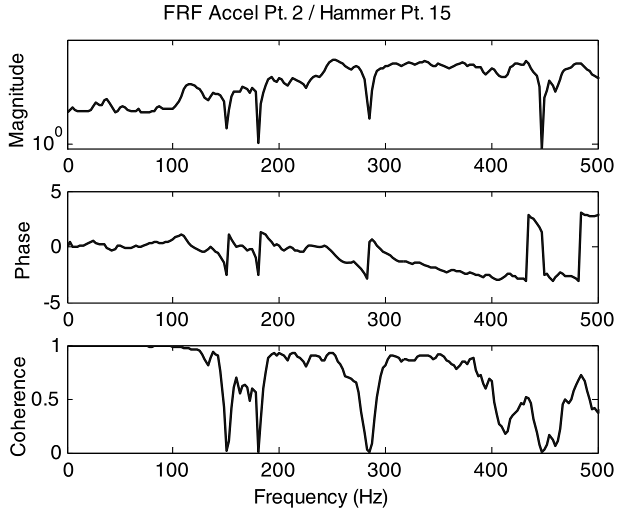

Fig. 4 Example of the frequency response function from the impact hammer test of a rectangular panel, zoomed 0–500 Hz.

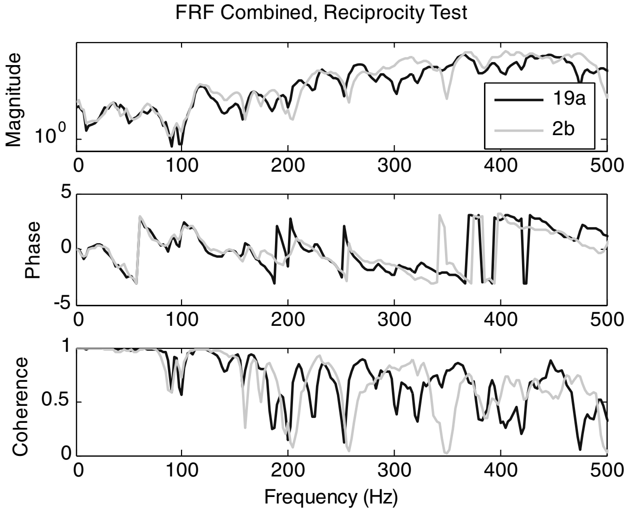

Fig. 5 Reciprocity test of impact hammer data.

linear structures will show nearly identical frequency response functions. Figure 5 reveals that the two reciprocal FRFs follow approximately the same path until around 250 Hz, at which point variation between the two appears. This indicates that the measured data is likely of usable quality below 250 Hz.

III. Individual Panel Dynamic Testing

The test setup in Fig. 6 was used to investigate the dynamic behavior of the rectangular stiff ultralightweight polyimide panel shown in Fig. 1. The panel was suspended horizontally by tensioning rubber bands attached to the panel and 1.5-m-long monofilament lines. The rubber bands were adhered to the panel with super glue without cutting or otherwise damaging the panel. This suspension method approximated a free–free boundary condition by limiting all rigid body suspension responses of the structure to a frequency range an order of magnitude less than the first structural natural frequency of the panel. In this case the “up-and-down” vertical suspension rigid body mode was counted visually to be approximately 2 Hz and the rocking mode approximately 3 Hz.

The hard, steel-tipped impact hammer shown in Fig. 6 was used to excite the structure and the response was measured by an accelerometer attached to the underside of the panel with super glue. The output cables from the hammer and accelerometer were both routed through a rack-mounted signal conditioner and recorded by the data acquisition system. Settings for the acquisition software used to collect the data and calculate the FRFs are shown in Table 1.

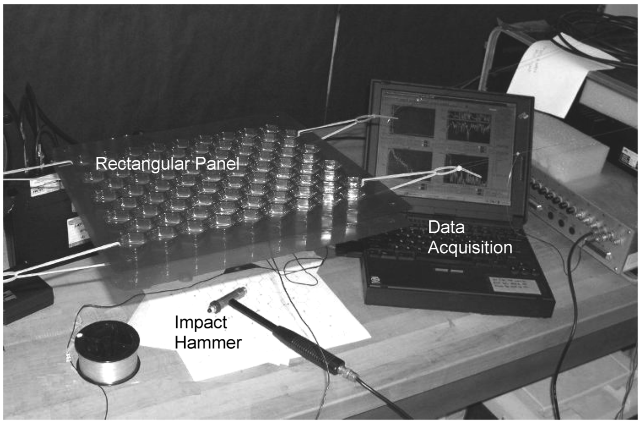

Fig. 6 Impulse dynamic test setup of single rectangular panel.

Forty-eight FRFs were collected by striking the top of the panel with the steel-tipped impact hammer at 24 excitation points (nodes) and measuring the response of the structure with the accelerometer attached to the underside of the panel at two of those excitation points. Only one accelerometer was attached to the panel at a time to avoid altering the mass properties of the panel. Therefore, two separate data runs were taken in which all 24 excitation points were struck, and the accelerometer was moved from one measurement point to the other in between runs. Each of the 24 excitation points was struck 20 times, and the data was averaged to create a single FRF. This number of averages was selected by observing the change in the computed FRF as more averages were added, and no change was observed beyond 20 averages. One of the 48 computed FRFs is shown in Figs. 3 and 4.

All 48 FRFs over the entire 0–2000 Hz bandwidth were combined and loaded into the modal parameter analysis software X-Modal. A modal parameter estimation was then performed using the eigensystem realization algorithm (ERA), a time-domain, high-matrix polynomial order algorithm that is numerically stable and recursively determines the order of the system based on Gram–Schmidt orthonormalization [13,14]. The first step in the modal parameter estimation process is to sieve the data, limiting the range over which the frequencies are estimated. After the frequency range is selected, the range of the time history is also limited. The parameter limiting the order of the function fit to the data, corresponding to the number of modes to be solved for and called NrVirtual in the software, is then selected, resulting in equation condensation.

After all of the parameters were selected, X-Modal created consistency diagrams that were used to determine the resonant frequencies. The consistency diagram used to determine the first two natural frequencies of the rectangular panel is shown in Fig. 7. Two FRFs are plotted here, indicating that two response points were used in the data collection. They are, however, simply for reference purposes because the ERA modal parameter estimation curve fits to all of the FRFs. Here the analyzed spectral content was sieved to between 40 and 130 Hz, the temporal content was set to include everything from the beginning of the measurement to just before the high-frequency noise at the end, and NrVirtual was set to 3. The identified resonances are therefore only calculated in the sieved frequency range and not the entire 2000 Hz bandwidth of the

Table 1 Data acquisition system settings

Setting	Value
Measurement bandwidth	0–2000 Hz
Frame size	2048
Number of averages	20
Δ frequency	2.5 Hz
Window	Exponential

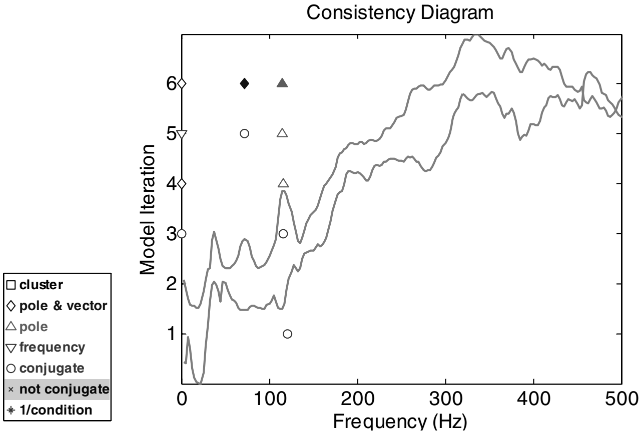

Fig. 7 Consistency diagram for rectangular panel testing using ERA, frequency range 40–130 Hz.

measurement. As the number of iterations increases, the model converges and the resonance frequencies are identified as indicated by solid symbols in the figure. These two frequencies represent the first and second structural natural frequencies of the rectangular panel, at 71.9 and 115.2 Hz, respectively. Note that both of these frequencies occur above the useful acoustic excitation range described previously.

After the frequencies were identified, a process was run in X-Modal to calculate the residues, a sample of which is shown in Fig. 8. Figure 8 shows the curve fit to the data over the sieved frequency range, and the error of the fit for this particular point. The deflection shapes corresponding to the selected frequencies at 71.9 and 115.2 Hz were then animated, single frames of which are shown in Figs. 9 and 10. The first mode shape in Fig. 9 is an edge view of a twisting mode in which adjacent corners of the panel are moving in opposite directions. The second mode shape in Fig. 10 shows a half sine wave along each edge of the panel, with opposite edges moving in the same direction in phase with each other, adjacent edges moving in opposite directions out of phase with each other, and little or no motion occurring in the center. These clean, clearly recognizable shapes confirm that the two frequencies selected from the consistency diagram in Fig. 7 are structural natural frequencies.

Following the successful extraction of the first two structural resonance frequencies and mode shapes, the data were reprocessed to determine if higher modes could also be extracted. The spectral content was sieved to between 117.5 and 300 Hz, the temporal content was set to include everything from the beginning of the measurement to just before the high-frequency noise at the end, NrVirtual was set to 3, and the generated consistency diagram was used to determine the third and fourth natural frequencies. These two frequencies represent the third and fourth structural natural frequencies of the structure, and were found to occur at 197.0 and 244.6 Hz, respectively.

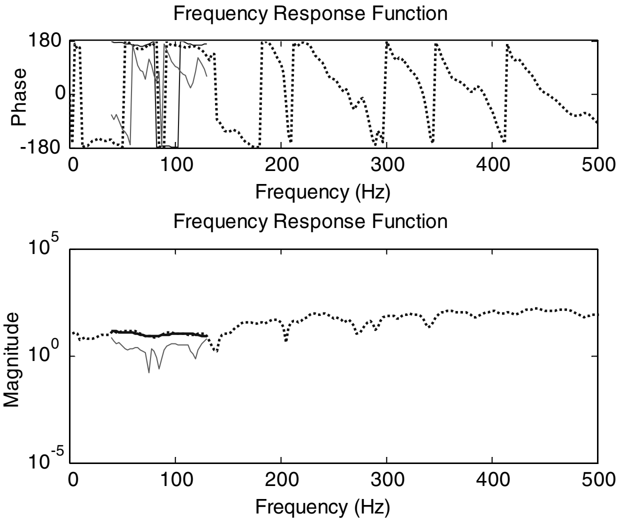

Fig. 8 Sample residue result in which the dotted line is the measured FRF, the heavy solid line is the reconstructed FRF, and the light solid line is the error.

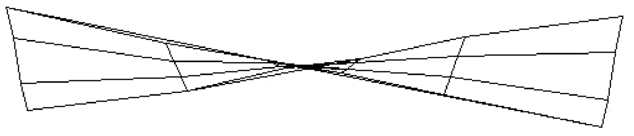

Fig. 9 Experimentally identified first mode shape of a rectangular panel at 71.9 Hz.

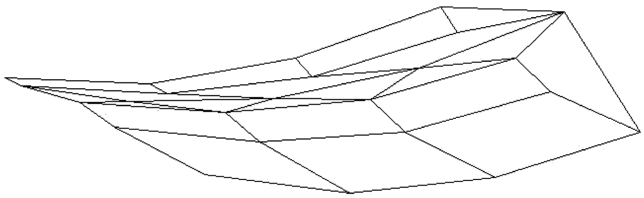

Fig. 10 Experimentally identified second mode shape of a rectangular panel at 115.2 Hz.

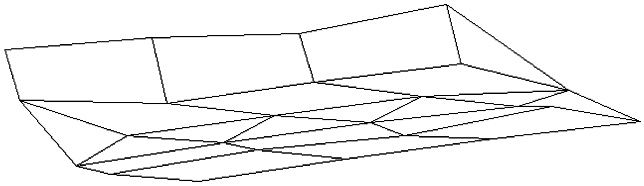

Fig. 11 Experimentally identified third mode shape of a rectangular panel at 197.0 Hz.

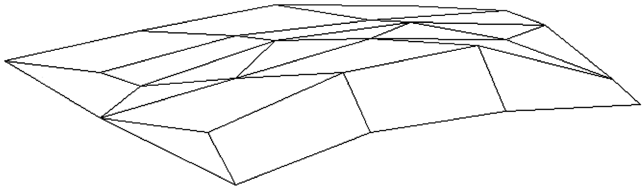

Fig. 12 Experimentally identified fourth mode shape of a rectangular panel at 244.6 Hz.

After the frequencies were identified, the process was run in X-Modal to calculate the residues. The deflection shapes corresponding to the selected frequencies at 197.0 and 244.6 Hz were then animated, single frames of which are plotted in Figs. 11 and 12. The third mode shape in Fig. 11 shows half sine waves along the short edges of the panel moving in opposite directions out of phase with each other and full sine waves along the long edges of the panel moving in the same direction in phase with each other. The fourth mode shape in Fig. 12 is difficult to identify from the individual frame, but appears as a third-order bending mode when animated. These clean, clearly recognizable shapes confirm that the two frequencies selected from the consistency diagram are structural natural frequencies.

Attempts at extracting additional structural resonance frequencies and mode shapes by sieving the data over other frequency ranges, including below 71 Hz and above 250 Hz, increasing the order of the function fit to the data, or any other method proved unsuccessful. The four successfully extracted structural resonance frequencies are listed in Table 2. It should be noted that all four fall within the range of useful data predicted by the reciprocity test in Fig. 5. The repetition of the third frequency at 197.0 Hz is due to the extraction of only one of the two orthogonal modes calculated in the finite element analysis discussed in the next section.

Table 2 Experimental and finite element structural natural frequencies of the individual panel

ANSYS mode number	ANSYS frequency, Hz	Experimental Frequency, Hz	ANSYS frequency 0.75ρ, Hz
7	62.659	7.9	72.353
8	99.884	115.2	115.34
9	175.13	197.0	202.22
10	183.39	197.0	211.76
11	247.46	244.6	285.74
12	348.41		402.31
13	435.74		503.15
14	462.03		533.51
15	523.62		604.63
16	562.86		649.94
17	588.7		679.77

Table 3 Defined properties for shell element models of stiff, ultralightweight polyimide panels

Panel dimensions	$25.0825 \times 26.67 \times 1.905$ cm
Panel mass	38.3 g
Volumetric density, ρ	30.0545 kg/m^3
Areal density	0.57 kg/m^2
Number of elements	1600
Number of nodes	1681
Stiffener spacing, t	0.3175 cm
Internal stiffener angle, θ	30 deg
Stiffener edge length, ℓ	$1.27 \cos(\theta)$ cm
Poisson's ratio xy, ν_{xy}	0.98
Poisson's ratio xz, ν_{xz}	0.34
Poisson's ratio yz, ν_{yz}	0.34
Apparent modulus, E_{app}	1.3318×10^8, 2.3179×10^8 Pa
Major and minor axis moduli, $E_x = E_y$	$2.3094 E_{\mathrm{app}} (t/\ell)^3$

IV. Individual Panel Finite Element Modeling and Correlation

Over the past several years, multiple attempts at using large, geometrically accurate, fine mesh shell element models to numerically simulate the behavior of ultralightweight membrane-dominated space structures [11,15–17], including a previous effort to model the semirigid polyimide panels in this study [18], have been undertaken. The prohibitively large size of these models and demonstrated linear quasi-static behavior of the panels in the previous section lead to an alternate approach here. Comparatively coarsely meshed, single layered shell element models of the panel tested above are proposed next for consideration. The material properties of the solid shell elements were defined to capture the behavior of the honeycomb geometry and unique hollow-walled construction of the panels (Fig. 13), yielding simple yet accurate models that can easily be applied to all of the experimental cases by modifying the global geometry [2,19].

A simple rectangle with a coarsely meshed single layer of four-node shell elements with material properties reflective of the unique honeycomb structure of the panel (Table 3) was used to replicate the experimental modal analysis data for the rectangular stiff ultralightweight polyimide panel [2]. To reflect the free–free test setup, no boundary conditions or constraints were applied to the model. A modal analysis was run, and the results are listed in Table 2. Note that the finite element solution returned the six rigid body modes that are excluded from Table 2, and that the table therefore starts numbering at mode seven. For comparison, the experimentally determined structural natural frequencies are also listed next to the finite element frequencies of identical mode shape.

Table 2 shows that the finite element model underpredicts the first three experimentally determined structural natural frequencies by 13, 13, 11, and 7%, respectively, and overpredicts the fourth by 1%. The third experimentally determined structural natural frequency is repeated; the ninth and tenth finite element modes both correspond to the third experimentally determined mode with one orthogonal to the other.

To achieve better correlation between the finite element and experimental data, the density defined in the model was altered. A finite element model density of 75% of actual was found to produce the best results, listed in Table 2, overpredicting the first two experimentally determined structural natural frequencies by just 0.7 and 0.09%, respectively. This density change equals a change in mass of the panel from 38.3 to 28.7 g. Note that to avoid this mass change, the modulus could be altered as an alternative, but density was chosen here because of the extensive effort required to calculate and measure the modulus of the panels [2]. The density used in the original finite element model was calculated by dividing the measured 38.3 g mass of the panel by the dimensions of the tessellating honeycomb structure, not the total dimensions of the film (Fig. 1). Only the dimensions of the honeycomb structure were modeled. Therefore the original model density overestimates the actual density of the modeled portion of the panel. This overestimation could be corrected with geometry changes to the model, addition of the excess material to the model, or removal of the excess material from the panel. In addition, other model refinements and modeling techniques could be investigated, such as a more detailed modeling of the boundary conditions, fluid effects, damping, and mass-loading of air [20] and an analysis of the internal stress fields, to generate models that do not require material property alterations. The density alteration used here demonstrates that the models can replicate the experimental data. Other refinements to achieve models that do not require such alterations are left to future work.

Direct comparisons of the first three simulated and experimentally determined mode shapes are shown in Figs. 14–16. Note that altering the density to achieve better agreement with the experimental data did not affect the shapes shown here. The comparison of first mode shapes in Fig. 14 shows edge views of identical twisting modes in which adjacent corners are moving in opposite directions. The comparison of second mode shapes in Fig. 15 shows identical half sine waves along each edge of the panels, with opposite edges moving in the same direction in phase with each other, adjacent edges moving in opposite directions out of phase with each other, and little or no motion occurring in the center. The comparison of third mode shapes in Fig. 16 shows identical half sine waves along the short edges of the panel moving in opposite directions out of phase with each other, and full sine waves along the long edges of the panel moving in the same direction in phase with each other.

The comparison of the first three finite element and experimentally determined mode shapes in Figs. 14–16 shows them to be quite similar. Therefore, the use of simple coarse-meshed shell element

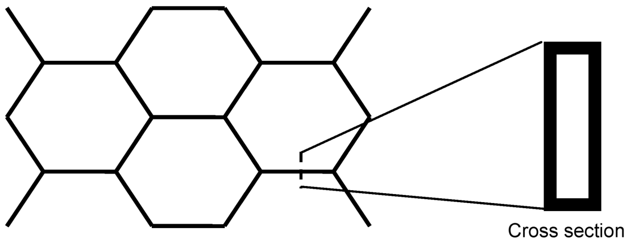

Fig. 13 Hollow-walled construction of stiff thermal-formed polyimide panels.

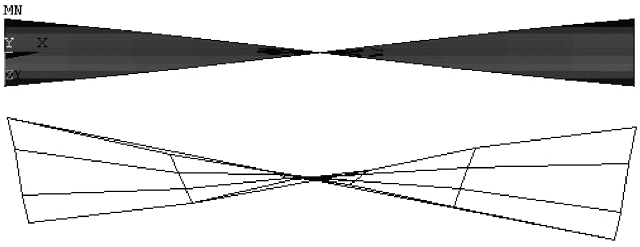

Fig. 14 Finite element (top) and experimentally determined (bottom) first mode shapes.

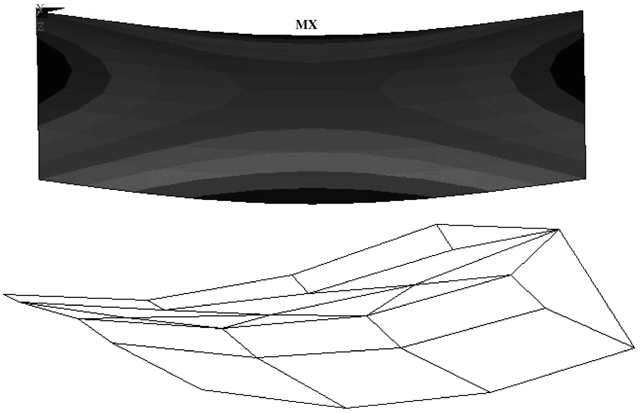

Fig. 15 **Finite element (top) and experimentally determined (bottom) second mode shapes.**

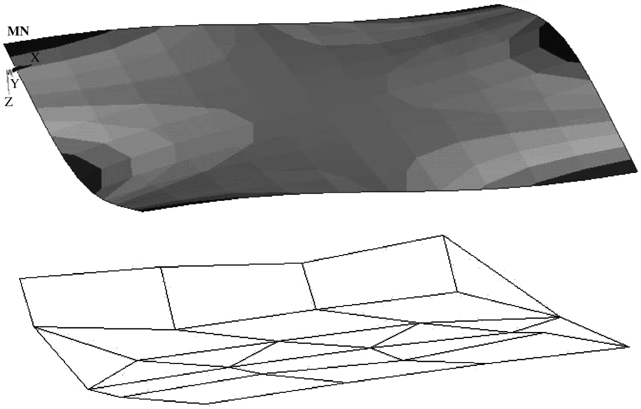

Fig. 16 **Finite element (top) and experimentally determined (bottom) third mode shapes.**

models to approximate the dynamic behavior of rectangular stiff, thermal-formed polyimide panels is possible and warrants further study. To demonstrate that the shell element models are effective at any size ranging from a single panel to the size of the full structure, an array of attached panels is tested and modeled next.

V. Multipanel Array Dynamic Testing

Investigation of the dynamic behavior of the array of joined rectangular panels shown in Fig. 17 was undertaken in the form of an experimental modal analysis of a cantilevered configuration. The array of three joined rectangular panels was cantilevered vertically as shown in Fig. 18, and impact excitation was used to dynamically excite its first four vibrational modes. The motion of the array following impact was recorded by the two synchronized monochromatic digital video cameras at rates as high as 75 frames per second, also shown in Fig. 18. Small circular, high-contrast retroreflective targets were attached to the array and table leg, and appear as bright white circles in Fig. 18. The targets were illuminated by flood lights placed directly behind the video cameras recording their motion so that the incident light was reflected directly back into the cameras. Actual images used in the processing are seen in Fig. 19. Here, the retroreflective targets appear as bright white circles on a dark, underexposed background created by the small aperture.

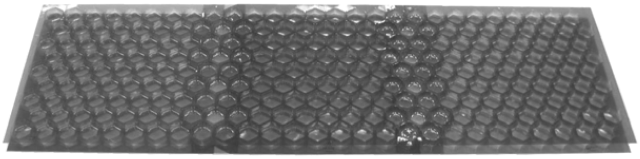

Fig. 17 **Array of attached rectangular panels.**

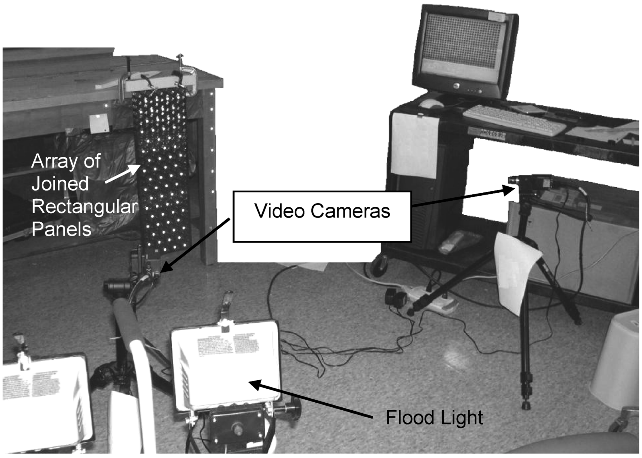

Fig. 18 **Dynamic test setup of cantilevered array.**

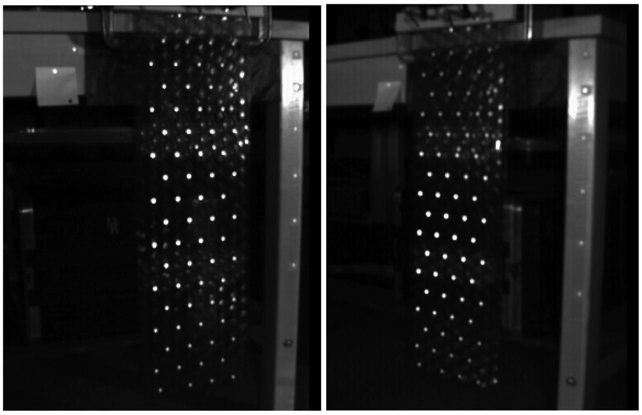

Fig. 19 **Actual images used in videogrammetry processing.**

The synchronized image sequences were then loaded into the PhotoModeler photogrammetry software package and associated with the appropriate camera calibration parameters, which allowed for the removal of image distortions caused by lens curvature and camera aberrations and imperfections. The targets were marked to subpixel accuracy (approximately $1/10$ pixel) using an automatic least-squares matching algorithm and referenced across the images to the marks corresponding to the same targets. A triangulation algorithm was run that simultaneously and iteratively solved for the three-dimensional locations of the targets and camera positions. The final product of the photogrammetry process was a set of three-dimensional points corresponding to the locations of the imaged retroreflective targets. This process was then applied to all of the synchronized image frames from the two video cameras to yield time histories of all the three-dimensional points [4,21–23]. The points on the table leg, visible in Figs. 18 and 19, were used to scale and rotate the data.

Four different points were impacted to excite the first and second bending and first and second twisting modes of the cantilevered array. For each desired mode, the array was impacted at the point of maximum deflection as follows [24]: at the free end and approximately halfway between the clamped and free ends, both in the middle of the array for the first and second bending modes, respectively; and at the free end and approximately halfway between the clamped and free ends, both at the edge of the array for the first and second twisting modes, respectively.

The time history data from the videogrammetry processing was then examined for spectral content [4,21]. Figure 20 shows a sample time history of a point in the first twisting mode shape test. The top graph of the figure shows the full time history recorded at 75 frames per second in which the impact did not occur for approximately one tenth of a second after video recording was initiated, and the

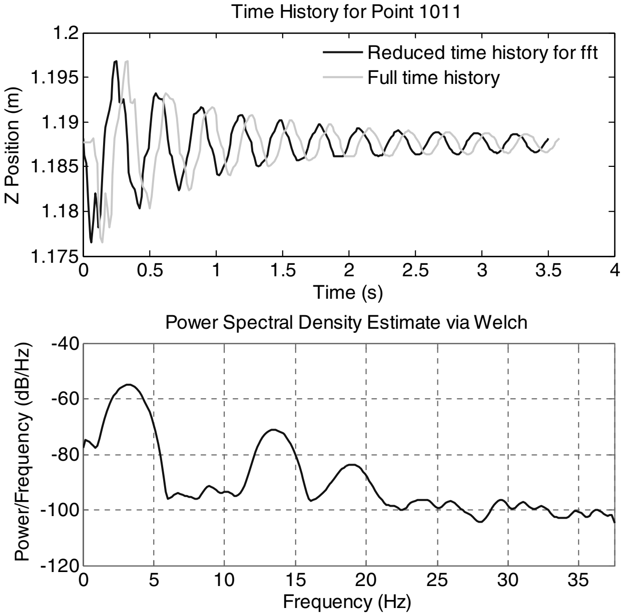

Fig. 20 Sample time history and power spectral density from the first twisting mode test.

reduced time history in which the information from before the impact is eliminated to enable the Fourier transform. The point exhibits a decaying harmonic oscillation, as expected from cantilevered impact testing. The power spectral density of the reduced time history (obtained via Fourier transform), shown in the bottom graph of Fig. 20, shows the frequency content of the signal. As expected, there is a peak at approximately 3.2 Hz, corresponding to the approximately 0.33 s period apparent in the temporal data. Note that in this study of the dynamic behavior of the array, only the spectral content of the response data is examined. The excitation is not incorporated as in the previous testing of the individual rectangular panels in which frequency response functions were examined.

To determine which shape this frequency corresponds to, a surface was fit to all of the points on the array in each synchronized measurement frame, called an epoch, and animated over all of the epochs. The animation clearly shows the first bending mode shape, one frame of which is shown in Fig. 21. Note that to enhance visualization, the data have been rotated to appear horizontal, and are not presented in their true vertical orientation.

To locate the remaining three desired modes, the spectral information from sample points on the array, such as that shown in Fig. 20, were examined, and the peaks corresponding to different modes were selected. A temporal filter was then applied to the response of all of the points on the array to eliminate spectral content outside of the desired frequency range. These data sets were recorded at 75 frames per second. In Fig. 22, only motion from 12 to 23 Hz was animated using a bandpass eighth-order Butterworth temporal filter of the data set in which the exact center of the array (maximum deflection location) was impacted to show the second bending mode shape. In Fig. 23, only motion from 11 to 16 Hz was animated using a bandpass eighth-order Butterworth temporal filter of the data set in which the edge of the array was impacted at the free end to show the first twisting mode shape. These two frequency ranges were selected to capture as much motion over as wide a spectrum as possible to ensure the desired shape was clearly visible. In Fig. 24, only motion above 30 Hz was animated using a high-pass eighth-order Butterworth temporal filter of the data set in which the edge of the array was impacted halfway between the free and clamped ends to show the second twisting mode shape. Because the maximum frame rate of the video cameras was 75 frames per second, spectral information was only available below Nyquist of 37.5 Hz and therefore the exact range of the peak corresponding to the second twisting mode could not be determined. It is still possible, however, to see from the animated shape that the second twisting motion is present, indicating that the mode occurs between 37.5 and 75 Hz.

The slight divot visible at approximately 1/4 of the panel length from the fixed end in Figs. 23 and 24 and most pronounced in Fig. 22 results from the glare of the flood lights on the surface of the array seen in the top portion of the array in the left image in Fig. 19. This glare resulted in inaccuracies in target marking throughout the videogrammetry data processing.

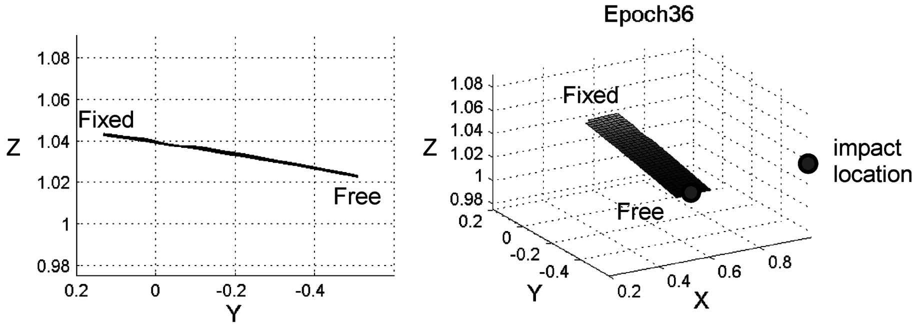

Fig. 21 Experimentally determined first mode shape at 3.2 Hz, impact at free end.

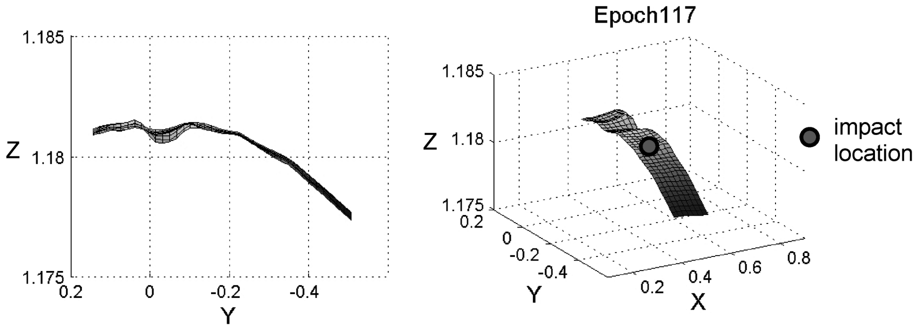

Fig. 22 Experimentally determined second bending mode shape, bandpass filter 12–23 Hz.

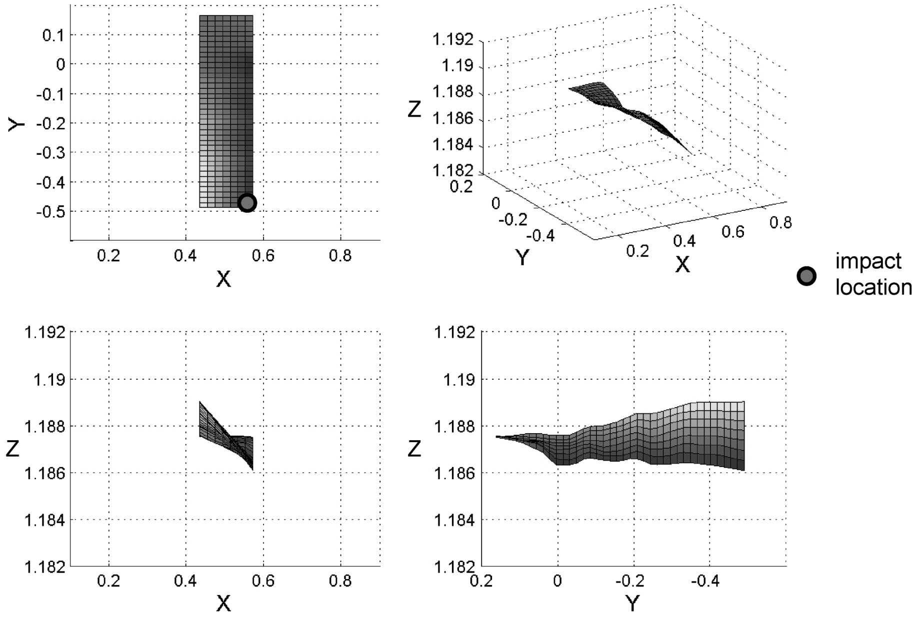

Fig. 23 Experimentally determined first twisting mode shape, bandpass filter 11–16 Hz.

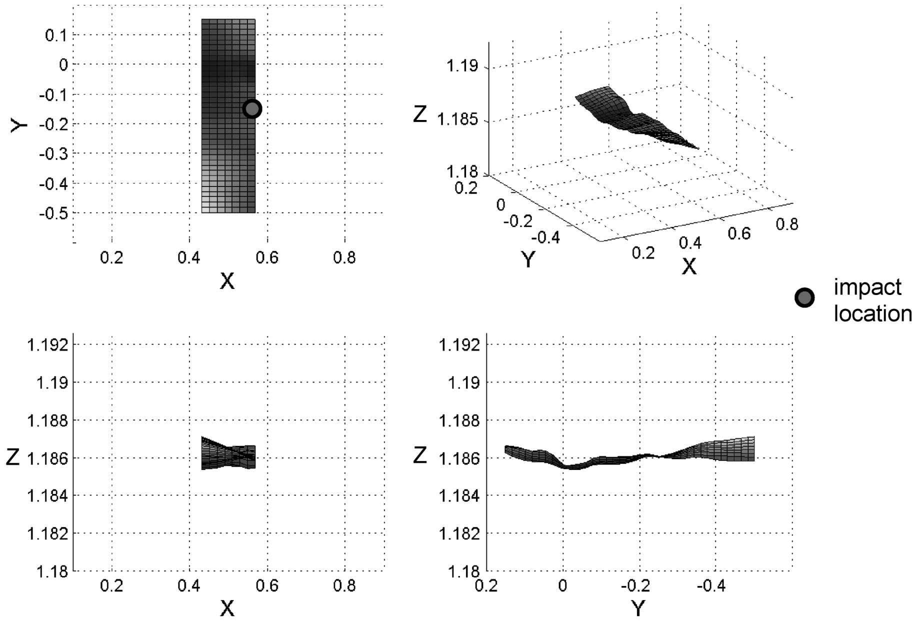

Fig. 24 Experimentally determined second twisting mode shape, high-pass filter 30 Hz.

The deflection shapes shown in Figs. 21–24 show that the peaks in the spectral data shown in Fig. 20 are structural natural frequencies of the array of joined rectangular panels. These frequencies are summarized in Table 4.

The temporal data from the impact testing of the array of joined panels can also be used to examine damping. Figure 25 shows a sample time history low-pass filtered to remove all frequency content above 8 Hz. The remaining decaying harmonic oscillation and its corresponding power spectral density show only the first mode behavior at approximately 3.2 Hz. In a linearly damped system, the rate at which the amplitude of the oscillating signal decays is an exponential function of the damping coefficient of the structure ζ that can be estimated by the logarithmic decrement method [25,26]. Therefore, from any given experimental decaying signal, such as the one in Figure 25, one can estimate the damping of the system. Figure 26 shows the results of the logarithmic decrement method applied to the low-pass filtered time history shown in Fig. 25. As often happens, damping estimates only yield a range of values of ζ, here from 6.5 to 11%. However, it can also be seen that fitting a linear (first-order) exponential curve to the peaks in the data also does not satisfactorily fit the decaying signal.

In Fig. 26, several exponential curves were fit to the peaks in the data, each of a different order. Again, the first-order linear curve does not perform satisfactorily, but the second-order nonlinear exponential is a good match to the decaying harmonic. This result indicates that the array of three joined rectangular panels exhibits complex nonlinear damping and may explain why the logarithmic decrement method was unsuccessful at providing an accurate damping estimate.

VI. Multipanel Array Finite Element Modeling and Correlation

A simple shell element finite element model nearly identical to that detailed in Sec. IV was used to model the cantilevered panel array. A 78.74 × 23.49 cm (31 × 9 in.) rectangle was meshed using the same 1.905-cm-thick (0.75-in.-thick) shell elements. Here, however, the upper 23.49 × 3.175 cm (9 × 1.25 in.) portion of the array was

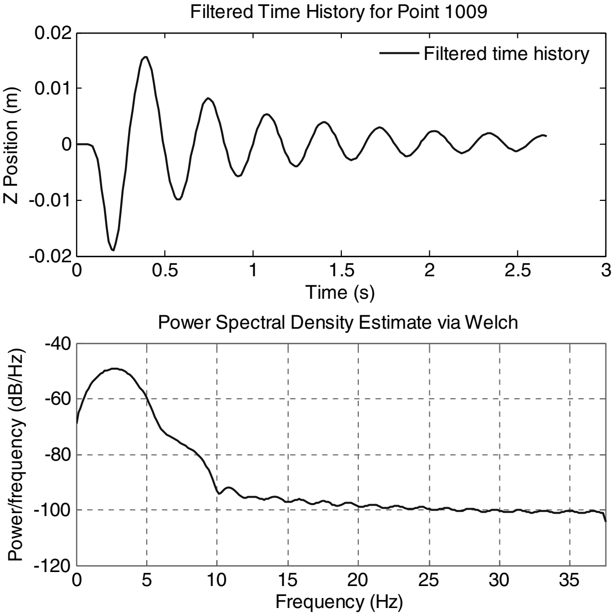

Fig. 25 Sample time history with low-pass filter at 8 Hz and power spectral density.

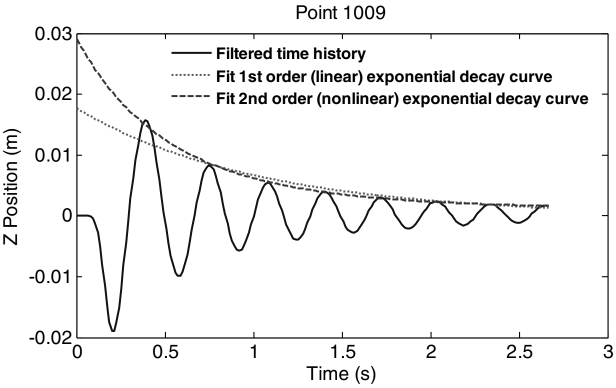

Fig. 26 Filtered time history with first- and second-order best fit damping estimates.

constrained to be fixed, matching the experimental boundary conditions. No load was applied to the model. A modal analysis was run, and the results are listed in Table 4. For comparison, the experimentally determined natural frequencies are also listed.

Table 4 shows that the finite element model overpredicts the first three experimentally determined structural natural frequencies by 6, 10, and 14%, respectively. The fourth finite element structural natural frequency is an in-plane mode not measured by the experimental data.

To achieve better correlation between the finite element and experimental data, the density defined in the model was altered. This procedure was used because the model did not reflect some of the experimental boundary conditions, specifically that to minimize crushing of the array, the C clamps used were not fully tightened. This possible clamp looseness, the small-scale nonlinear stiffness behavior of the panel [4], and experimental uncertainty make it impossible that the clamp was ideal in the experimental data set. It is therefore likely that some motion at the base of the array did occur. To correct for these unmodeled effects, the density used in the defined material properties was increased until a suitable match with the experimental data was achieved. Ultimately, 110% of actual density was found to produce excellent agreement with the measured structural natural frequencies, also listed in Table 4, overpredicting the first three experimentally determined frequencies by just 1, 6, and 8%, respectively. This density change equals a change in mass of the array from 81.4 to 89.5 g. Other model refinements and modeling techniques could be investigated, such as a more detailed modeling of the boundary conditions, air damping, and analysis of the internal stress fields, to generate models that do not require material property alterations. The density alteration used here demonstrates that the models can replicate the experimental data. Other refinements to achieve models that do not require such alterations are left to future work.

Direct comparisons of the first three simulated and experimentally determined mode shapes are shown in Figs. 27–30. Note that altering the density to achieve better agreement with the experimental data did not affect the shapes, and that to enhance visualization the data have been rotated to appear horizontal rather than the actual vertical orientation. Also note that the finite element shapes include the portion of the array underneath the clamp, whereas the experimental shapes do not. The comparison of first mode shapes in Fig. 27 show comparable first beam bending modes. The comparison of second mode shapes in Fig. 28 shows comparable first beam twisting modes. The comparison of third mode shapes in Fig. 29 shows comparable second beam bending modes. The comparison of fourth mode shapes in Fig. 30 shows an ideal second twisting mode from the finite element simulation and what appears to be a second twisting mode from the experimental data. Because the mode occurred above Nyquist, a specific range of bandpass filtering could not be used on the experimental data. Therefore, more high-frequency noise is present in the displayed shape than in the other experimental shapes, making it difficult to clearly match the experimental and finite element shapes.

The comparison of the three finite element and experimentally determined mode shapes in Figs. 27–29 shows them to be well correlated. Therefore, the use of simple coarsely meshed shell element models to approximate the dynamic behavior of an array of joined rectangular panels is shown to be possible.

VII. Conclusions

Noncontact excitation and measurement techniques used successfully in the testing of past ultralightweight membrane structures were investigated here for use in the dynamic characterization of the panels. It was determined, however, that more standard impact hammer excitation and accelerometer measurements were better able to extract the first four structural natural frequencies and mode shapes of the panels than the other techniques. This setup was used to characterize the dynamic behavior of the first four modes at 71.9, 115.2, 197.0, and 244.6 Hz of an individual rectangular panel. The linear dynamic behavior enabled the use of simple coarsely meshed modified shell element

Table 4 Experimental and finite element structural natural frequencies of the array

ANSYS mode number	ANSYS frequency, Hz	Experimental frequency, Hz	ANSYS frequency 1.10ρ, Hz	Description
1	3.389	3.2	3.231	First bending
2	14.813	13.5	14.123	First twisting
3	21.559	19.0	20.556	Second bending
4	30.033	n/a	28.635	First in plane
5	48.096	>37.5	45.858	Second twisting

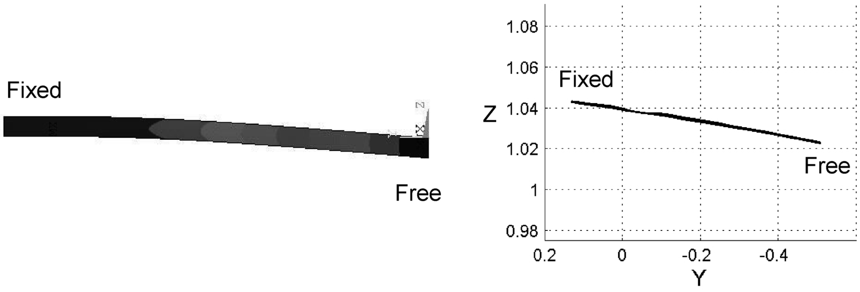

Fig. 27 Finite element (left) and experimentally determined (right) first mode shapes.

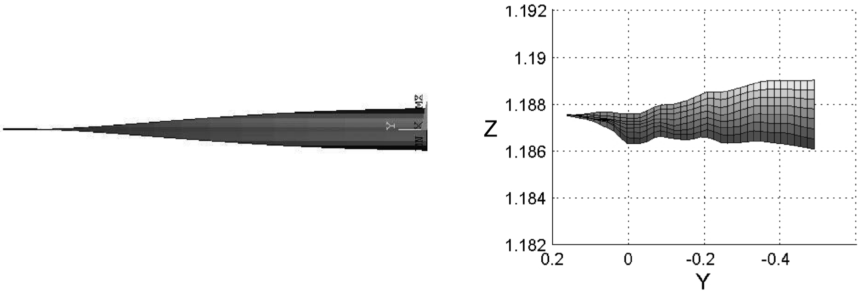

Fig. 28 Finite element (left) and experimentally determined (right) second mode shapes.

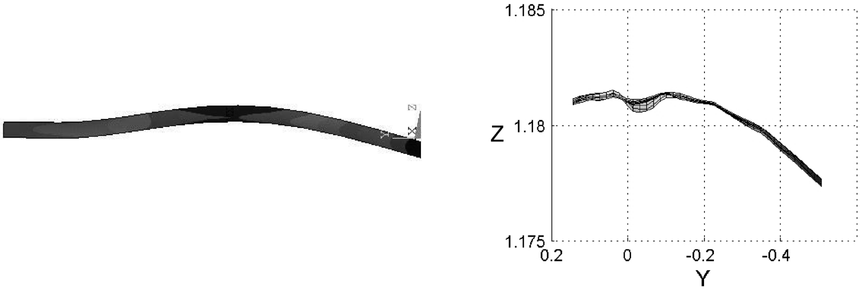

Fig. 29 Finite element (left) and experimentally determined (right) third mode shapes.

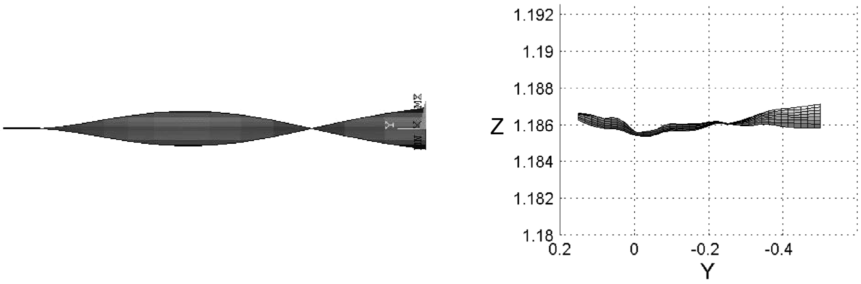

Fig. 30 Finite element (left) and experimentally determined (right) fourth mode shapes.

models to capture the large-scale dynamic panel behavior. The modification involved altering the modulus of the shell elements to reflect the unique internal honeycomb structure of the panels and thermal-formed polyimide film from which the panels are manufactured.

The dynamic behavior of the array of attached panels was also investigated through cantilevered impact testing. The response of the array was recorded and processed using videogrammetry, yielding the three-dimensional time history behavior of the panel. Filtering was applied to the data to remove all motion outside of specific frequency ranges and, in this manner, the deflection shapes of the array and corresponding resonant frequencies of the first three modes at 3.2, 13.5, and 19.0 Hz were extracted. The modified coarsely meshed shell elements used in the individual rectangular panel modeling accurately predicted the measured dynamic behavior of the array.

Future modeling work should involve comparing the simple coarsely meshed finite element models used successfully here with more complicated models to characterize a model size to accuracy tradeoff. Future testing should include vibration testing under a vacuum to determine the effect of air mass loading and damping on the modal properties of the panels, as well as an exploration of alternate excitation methods such as piezo patches to extract more natural frequencies.

Acknowledgements

This work is a portion of a Ph.D. dissertation through the University of Kentucky, Suzanne Weaver Smith and Jack Leifer advisors, and George Blandford and Kozo Saito committee members. It was performed under a NASA Graduate Student Research Program fellowship, grant NNL04AA21H, Richard Pappa advisor, and a NASA Small Business Innovation Research grant, Larry Bradford Principal Investigator. The views expressed in this article are those of the authors and do not reflect the official policy or position of the United States Air Force, Department of Defense, or the U.S. Government.

References

[1] Black, J. T., Smith, S. W., and Leifer, J., "Reduced Model Validation of Thermal-Formed Polyimide Panels," *Proceedings of the 25th International Modal Analysis Conference*, Society for Experimental Mechanics, Inc., Bethel, CT, Feb. 2007.

[2] Black, J. T., "New Ultra-Lightweight Stiff Panels for Space Apertures," Ph.D. Dissertation, Dept. of Mechanical Engineering, Univ. of Kentucky, Dec. 2006, http://lib.uky.edu/ETD/ukymeen2006d00532/BlackDis.pdf [retrieved 1 Dec. 2007].

[3] Pappa, R. S., Lassiter, J. O., and Ross, B. P., "Structural Dynamics Experimental Activities in Ultralightweight and Inflatable Space Structures," *Journal of Spacecraft and Rockets*, Vol. 40, No. 1, 2003, pp. 15–23.

[4] Pappa, R. S., Black, J. T., Blandino, J. R., Jones, T. W., Danehy, P. M., and Dorrington, A. A., "Dot Projection Photogrammetry and Videogrammetry of Gossamer Space Structures," *Journal of Spacecraft and Rockets*, Vol. 40, No. 6, 2003, pp. 858–867.

[5] Johnston, J. D., Blandino, J. R., and McEvoy, K. C., "Analytical and Experimental Characterization of Gravity Induced Deformations in Subscale Gossamer Structures," *Journal of Spacecraft and Rockets*, Vol. 43, No. 4, 2006, pp. 762–770.
doi:10.2514/1.14298

[6] Flint, E., Bales, G., Glaese, R., and Bradford, R., "Experimentally Characterizing the Dynamics of 0.5 m+ Diameter Doubly Curved Shells Made From Thin Films," AIAA Paper 2003-1831, April 2003.

[7] Flint, E. M., Lindler, J. E., Hall, J. L., Rankine, C., and Regelbrugge, M., "Overview of Form Stiffened Thin Film Shell Characteristic Behavior," AIAA Paper 2006-1900, May 2006.

[8] Song, H., Smith, S. W., and Main, J. A., "Dynamic Testing of an Inflatable, Self-Supporting, Unpressurized Thin Film Torus," *Journal of Guidance, Control, and Dynamics*, Vol. 29, No. 4, 2006, pp. 839–845.

[9] Griffith, D. T., and Main, J. A., "Experimental Modal Analysis and Damping Estimation of an Inflated Thin-Film Torus," *Journal of Guidance, Control, and Dynamics*, Vol. 25, No. 4, 2002, pp. 609–617.

[10] Ruggiero, E. J., Park, G., and Inman, D. J., "Multi-Input Multi-Output Vibration Testing of an Inflatable Torus," *Mechanical Systems and Signal Processing*, Vol. 18, No. 5, 2004, pp. 1187–1201.
doi:10.1016/j.ymssp.2004.01.003

[11] Lore, K., and Smith, S. W., "Efficient Computation of Dynamic Response of Large Flexible Spacecraft," AIAA Paper 2005-2051, April 2005.

[12] Bennighof, J. K., Kaplan, M. F., and Muller, M. B., "Extending the Frequency Response Capabilities of Automated Multi-Level Substructuring," AIAA Paper 2000-1574, April 2000.

[13] Juang, J. N., and Pappa, R. S., "An Eigensystem Realization Algorithm for Modal Parameter Identification and Model Reduction," *Journal of Guidance, Control, and Dynamics*, Vol. 8, No. 5, 1985, pp. 620–627.

[14] Longman, R. W., and Juang, J. N., "Recursive Form of the Eigensystem Realization Algorithm for System Identification," *Journal of Guidance, Control, and Dynamics*, Vol. 12, No. 5, 1989, pp. 647–652.

[15] Wang, J. T., and Johnson, A. R., "Deployment Simulation of Ultra-Lightweight Inflatable Structures," AIAA Paper 2002-1261, 2002.

[16] Tesseler, A., Sleight, D. W., and Wang, J. T., "Nonlinear Shell Modeling of Thin Membranes with Emphasis on Structural Wrinkling," AIAA Paper 2003-1931, 2003.

[17] Su, X., Abdi, F., Taleghani, B., and Blandino, J. R., "Wrinkling Analysis of a Kapton Square Membrane Under Tensile Loading," AIAA Paper 2003-1985, 2003.

[18] Black, J. T., Smith, S. W., and Leifer, J., "Investigating Semi-Rigid Kapton Panels for Use in Space Telescopes," International Astronautical Congress Paper IAC-05-C2.1.B.05, Oct. 2005.

[19] Gibson, L. J., and Ashby, M. F., *Cellular Solids: Structures and Properties*, Pergamon, New York, 1988, ISBN 0-08-036607-4.

[20] Kukathasan, S., and Pellegrino, S., "Vibration of Prestressed Membrane Structures in Air," AIAA Paper 2002-1368, 2002.

[21] Black, J., "Photogrammetry and Videogrammetry Methods Development for Solar Sail Structures," M.S. Thesis, Joint Inst. for Advancement of Flight Sciences, NASA Langley Research Center, George Washington Univ., Washington, D.C., Aug. 2003;also NASA CR-2003-212678, Sept. 2003.

[22] Black, J. T., Leifer, J., DeMoss, J. A., and Walker, E. N., "Experimental and Numerical Correlation of Gravity Sag in Solar Sail Quality Membranes," *Journal of Spacecraft and Rockets*, Vol. 44, No. 3, 2007, pp. 522–527.
doi:10.2514/1.20958

[23] Leifer, J., Black, J. T., Smith, S. W., Ma, N., and Lumpp, J. K., "Measurement of In-Plane Motion of Thin-Film Structures Using Videogrammetry," *Journal of Spacecraft and Rockets*, Vol. 44, No. 6, Nov.–Dec. 2007, pp. 1317–1325 ; also AIAA Paper 2006-1805, 2006.

[24] Blevins, R. D., *Formulas for Natural Frequency and Mode Shape*, Krieger, Malabar, FL, 1979, ISBN 1575241846.

[25] Thompson, W. T., and Dahleh, M. D., *Theory of Vibration with Application*, 5th ed., Prentice–Hall, Upper Saddle River, NJ, 1993, ISBN 0-13-651068-X.

[26] Ewins, D. J., *Modal Testing: Theory and Practice*, Research Studies Press, Ltd., Somerset, England, 1984, ISBN 0863800173; also Wiley, New York, 1984, ISBN I0471904724.